

Numerical modelling of aeolian erosion over a surface with non-uniformly distributed roughness elements

B. Furieri,^{1,2*} J. L. Harion,^{1,2} M. Milliez,³ S. Russeil^{1,2} and J. M. Santos⁴

¹ Université Lille Nord de France, F-59000 Lille, France

² Mines Douai, EI, F-59500 Douai, France

³ CERE, EDF R&D, Ecole des Ponts ParisTech, Université Paris Est, F-78401 Chatou, France

⁴ Universidade Federal do Espírito Santo, DEA, 29060-970 Vitória, ES, Brazil

Received 24 October 2012; Revised 1 April 2013; Accepted 18 April 2013

*Correspondence to: Bruno Furieri, Université Lille Nord de France, F-59000 Lille, France. E-mail: furieribruno@gmail.com

ESPL

Earth Surface Processes and Landforms

ABSTRACT: The present study is focused on the analysis of the mean wall friction velocity on a surface including roughness elements exposed to a turbulent boundary layer. These roughness elements represent non-erodible particles over an erodible surface of an agglomeration of granular material on industrial sites. A first study has proposed a formulation that describes the evolution of the friction velocity as a function of geometrical parameters and cover rate with different uniform roughness distributions. The present simulations deal with non-uniform distributions of particles with a random sampling of diameters, heights, positions and arrangements. The evolution (relative to geometrical parameters of the roughness elements) of the friction velocity for several non-uniform distributions of roughness elements was analysed by the equation proposed in the literature and compared to the results obtained with the numerical simulations. This comparison showed very good agreement. Thus, the formulation developed for uniform particles was found also to be valid for a larger spectrum of particles noted on industrial sites. The present work aims also to investigate in detail the fluid mechanics over several roughness particles. Copyright © 2013 John Wiley & Sons, Ltd.

KEYWORDS: wind erosion; non-erodible particles; roughness elements; CFD; open-source simulations; wall shear stress assessment

Introduction

This work is within the framework of environmental effects caused by the aeolian erosion of granular materials (e.g. coal, iron) commonly encountered on industrial sites. Diffuse sources generated by aeolian erosion events have motivated several studies (Zobeck and Sterk, 2003; Castel, 2006; Roney and White, 2006, 2010; Badr and Harion, 2007; Guingo and Minier, 2008; Neuman *et al.*, 2009; Ferreira and Lambert, 2011; Furieri *et al.*, 2012; Turpin and Harion, 2010), as have quantitative analyses of atmospheric pollution events. In many of these cases, mathematical models have been employed. The models commonly encountered for the quantification of dust emissions from diffuse sources present a lack of information regarding the effects of coarse particles on the decrease of emitted mass flux, the interactions between nearby sources and the various kinds of buildings that surround the sources, atmosphere stability, etc.

Thus the present study focuses on the local analysis of an erodible surface exposed to wind erosion in the presence of coarse particles found on granular material agglomerations. These particles are treated in our study as roughness elements over a smooth surface. For a given wind velocity, an agglomeration of granular material with a large size distribution is a mixing of erodible and non-erodible particles (Gillette and Stockton, 1989; McKenna-Neuman and Nickling, 1995; Neuman, 1998;

Al-Awadhi and Willetts, 1999; Gimenez *et al.*, 2006; Lopez *et al.*, 2007; Jiang *et al.*, 2008; Webb and Strong, 2011; Benkhaldoun *et al.*, 2012). By definition, the erodibility of particles submitted to aeolian erosion depends on the incoming wind flow velocity and their diameter. Non-erodible particles do not take-off from the surface because of their inertia.

The analysis of an erodible surface in the presence of non-erodible particles exposed to a turbulent wind flow is usually carried out by means of the wall shear stress repartition over the erodible surface. This approach was introduced, for roughness studies, by Schlichting (1968). The total stress (τ) is split into τ_R , the stress on roughness elements (non-erodible particles) and τ_S , the stress on the underlying surface.

Earlier investigations have shown that the soil wind erosion is strongly attenuated by the presence of non-erodible particles. The near fluid flow over erodible surfaces in the presence of non-erodible particles (roughness elements) has been widely studied (Raupach *et al.*, 1993; McKenna-Neuman and Nickling, 1995; King *et al.*, 2005; Shao and Yang, 2005; Gillies *et al.*, 2007; Turpin *et al.*, 2010) and can be summarized by the following points:

- increase of the threshold friction velocity;
- decrease of the mean friction velocity over the erodible surface and consequently of the soil erodibility; and
- temporal decrease of the emitted mass flux.

In fact, a phenomenon commonly called the pavement effect occurs as the non-erodible particles emerge on the erodible surface and finally cover the whole surface. Thus the erodible particles are no longer exposed to wind flow. The protection is characterized by the decrease of the mean shear stress on the underlying surface. Some geomorphological studies have discussed this phenomenon on various landforms and their effects on particle deposition and erosion. Typically, it may be called lag deposit (Davidson-Arnott *et al.*, 1997; Mountney and Russell, 2004; Hugenholtz *et al.*, 2009; Bullard and Austin, 2011; Buynevich, 2012; McKenna-Neuman *et al.*, 2012).

The purpose of this work is to continue the original research initiated by Turpin *et al.* (2010) for uniform particles. Numerical simulations were performed, from which a mathematical formulation was proposed to associate the geometrical characteristics of the non-erodible particles and the mean friction velocity of the erodible surface. In brief, the above-mentioned formulation proposes an evolution of the value of the friction velocity on the underlying surface (i.e. applied to erodible particles) as a function of roughness element parameters.

The formulation developed by Turpin *et al.* (2010) is presented in Equations (1) and (2) (see Definition of Symbols used in Table I):

$$R_{\text{fric}} = \frac{u_R^*}{u_S^*} \quad (1)$$

$$1 - R_{\text{fric}} = a_p \cdot (\text{TDC})^{m_p} \cdot (S_{\text{frontal}}/S_{\text{floor}})^{n_p} \quad (2)$$

where, in Equation (1), u_R^* and u_S^* are the friction velocities for, respectively, rough and smooth walls. In Equation (2), TDC is the cover rate, $S_{\text{frontal}} = bh_{\text{NEP}}$ and $S_{\text{floor}} = \pi b^2/4$ are respectively the frontal and the basal areas of a roughness element represented by a cylindrical non-erodible particle (b and h_{NEP} are the particle diameter and height, respectively), and a_p , m_p and n_p are empirical coefficients determined by the uniform numerical simulations carried out in the previous study. The coefficients depend on the range of particle parameters.

The formulation proposed by Turpin *et al.* (2010) was achieved after several similar numerical simulations. It was found that the parameter $1 - R_{\text{fric}}$ increases with the increase of $P_{\text{fric}} = \text{TDC} (S_{\text{frontal}}/S_{\text{floor}})$ in two different ways: higher slope when P_{fric} is between 0 and 2 and a smaller slope when P_{fric} is between 2 and 8. This behaviour is linked to the modification of the flow regime due to a modification of the roughness elements distribution. This modification observed in the flow behaviour was also previously discovered by Lee and Soliman (1977). Therefore the coefficients in Equation (2) depend on the range of P_{fric} .

In the present paper, the range of cases to be simulated was based on the same limits imposed by Turpin *et al.* (2010) for their formulation: the parameter P_{fric} is equal to a maximum of 8, which covers a large range of particles in nature.

Despite the contribution of the formulation to improving the understanding of the impacts of the non-erodible particles and the manner in which the friction velocity is accounted for, the formulation still presents a restriction. The numerical simulations carried out by Turpin *et al.* (2010) suppose that all the roughness elements show the same emerging level and have the same diameter. However, on industrial sites, the uniform condition is very rarely accomplished. It would therefore be useful to evaluate the robustness of the formulation proposed by Turpin *et al.* (2010) (Equation (2)), using the same parameters and coefficients for a non-uniform roughness element distribution and to identify any necessary modifications required.

For each simulation in the present study, particle diameters and heights are randomly chosen from a defined range of values. Numerical simulations were carried out with the open source

Computational Fluid Mechanics (CFD) code *Code_Saturne* (Archambeau *et al.*, 2004). It is worth noting that the present work will exclusively investigate cylindrical particles, as they are more representative of the fully random pattern observed on industrial sites than are spherical particles. In addition, particular attention is paid to the fluid mechanics analysis over a surface presenting roughness elements. The effects of roughness particles are important for the turbulent pattern of the wind flow (Lee and Soliman, 1977; Li and Martz, 1995; Kurose and Komori, 2001; Carney *et al.*, 2005; Orlandi and Leonardi, 2008; Sutton and Neuman, 2008). This investigation aims to improve the manner in which some models take into account changes in the influence of non-erodible particles on sediment transport.

Numerical Simulations

Geometry, meshing and boundary conditions

All the results presented in this study were obtained by means of numerical simulations. The three-dimensional (3D) equations of mass and momentum governing the phenomena were computed with the open source code *Code_Saturne* (Archambeau *et al.*, 2004), which is based on a finite-volume approach for co-located variables on an unstructured grid. It can handle complex geometries and physics. In our numerical simulations, we used a steady Reynolds average Navier Stokes (RANS) approach and turbulence effects were accounted for by using the $k-\omega$ shear stress transport (SST) model without wall functions for the turbulence damping near walls.

Figure 1a shows the computational domain and boundary conditions. The non-uniform pattern of the numerical simulations can be noted in Figure 1. For all tested configurations, the domain is a rectangular box. The base is a square of 30 mm and the height is 100 mm. The dimensions of the base of the computational domain were chosen to be statistically representative of the repetition pattern of the particles: flow pattern and turbulent characteristics. Badr (2007) has validated these dimensions for a uniform configuration with non-erodible elements with diameters of 1.0–3.0 mm and cover rates up to 20%. Later in the present work, a comparison of the impact of different spatial distributions of particles under the same flow conditions is presented to validate the domain dimensions for non-uniform configurations.

A periodic boundary condition is applied in the streamwise flow direction, since the pattern of the flow solution is expected to be periodic (Turpin *et al.*, 2010). In this way, the mass flow is fixed for a corresponding mean longitudinal velocity value equal to 8 m s^{-1} . For the upper boundary condition and laterals, symmetries are imposed to reduce computational efforts. Smooth walls with no-slip conditions are set at roughness elements and ground walls.

Meshing and turbulence modelling choices were based on previous similar numerical calculations carried out by Turpin *et al.* (2010). Figures 1b and c present the meshing details. The mesh is produced by an extrusion from triangular cells defined on the erodible surface and roughness elements walls (see Figure 1b) towards the interface boundary of the computational domain. Indeed, the calculation domain was divided into two parts with an interface at a height equal to three times the largest diameter (see Figure 1c). The use of an interface makes it possible to mesh the upper part with quadrilateral elements for better computational efficiency. Near the particles and the walls the mesh was constructed with hexahedral and pentahedral elements for a good refinement in the spanwise and streamwise directions. As required by

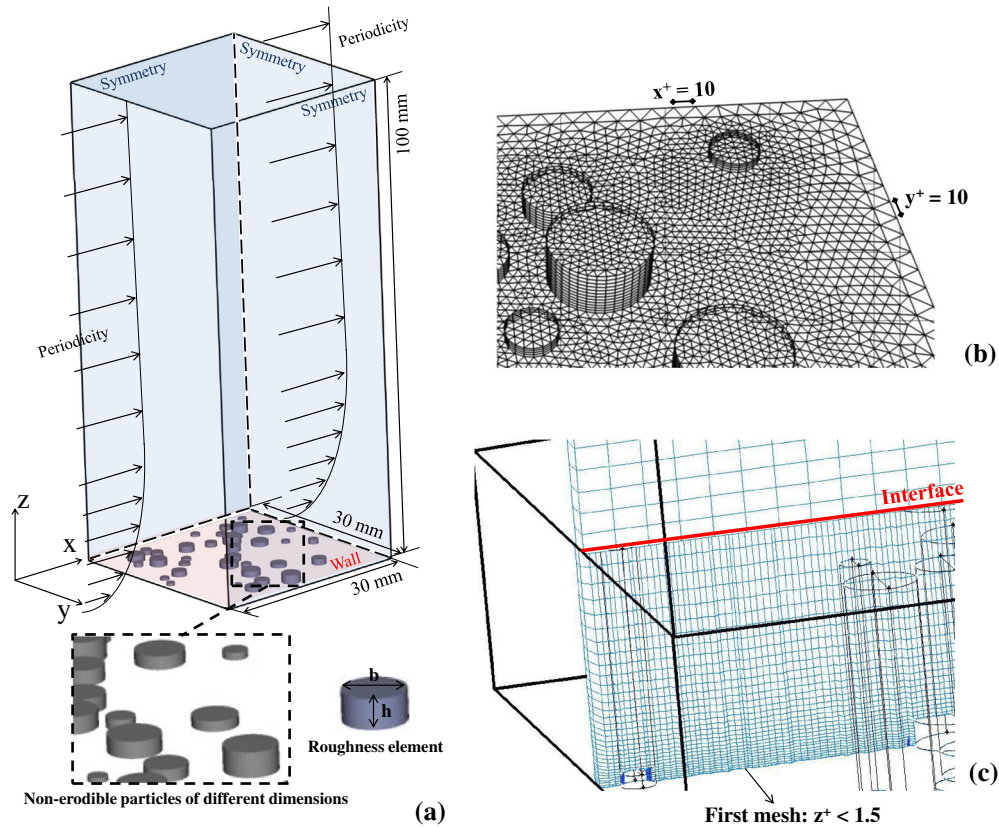


Figure 1. Computational domain: (a) dimensions and boundary conditions; (b) mesh on the wall of the erodible surface and roughness elements; (c) vertical mesh distribution. This figure is available in colour online at wileyonlinelibrary.com/journal/espl

the closure of the turbulence model, there is a mesh refinement near the wall surface where $z^+ \leq 1.5$ (to ensure no use of wall functions) based on the friction velocity for the smooth case.

It is worth noting that the numerical simulations performed by Turpin *et al.* (2010) were validated with previous numerical and experimental studies concerning roughness elements. The same comparison and validation is performed in the present study (Figure 2). The comparison plots the ratio of threshold friction velocity $R_t = u_{t-r}^*/u_{t-s}^*$ versus the roughness density $\lambda = N_p b h_{NEP} / S_{NEP}$ in logarithmic representation.

The roughness density λ was defined by Marshall (1971) and stated that the shear stress partition depends primarily on the roughness density parameter λ and to a lesser extent on roughness shape and distribution. With our numerical results the same mean behaviour was found:

$$R_t = \frac{u_{t-r}^*}{u_{t-s}^*} = \left[\frac{1}{(1 - m\sigma\lambda)(1 + m\beta\lambda)} \right]^{1/2} \quad (3)$$

where β is the ratio of the drag coefficient C_R of an isolated roughness element on the surface to the drag coefficient C_S of the substrate surface itself. Values for C_R are approximately 0.25 for cylinders (Taylor, 1988) and values for C_S have been reported to be approximately 0.0025 (Crawley and Nickling, 2003). σ is the basal-to-frontal area ratio of the roughness elements, and $m < 1$ is a parameter accounting for differences between the average substrate surface stress and the maximum stress on the surface at any point (see Turpin *et al.*, 2010, for more details).

A comparison was performed between the numerical data of Turpin *et al.* (2010) and those presently obtained with the above-mentioned numerical model *Code_Saturne* for the same uniform configurations. These extra simulations make sure that the code and numerical model used in the present

work give the same results as previously taken into consideration to construct the formulation. Table II presents the three uniform configurations simulated with *Code_Saturne* and previously with Fluent in Turpin *et al.* (2010). Good agreement was found for the values of $1 - R_{fric}$ calculated with the two codes. The three cases were chosen to represent very different particle distributions. These results are plotted in Figure 3a as filled circles and triangles.

Two additional simulations were performed (beyond the tests presented in Table III) to validate the representativeness of the computational domain: for the same values of TDC and $(S_{frontal}/S_{floor})$, the geometry parameters were changed (particle heights, diameters and distribution). The values of $1 - R_{fric}$ computed with the numerical results show a maximum difference of 5.2% between the tested cases. This low difference validates the domain dimensions and we may consider that it is well representative of the repeatability found in nature.

Tested configurations

Several configurations of non-uniform particles were carried out and are listed in Table III. The parameters that define each test are:

- range of particle diameters (b);
- mean diameter (\bar{b});
- range of particle heights (h_{NEP} as a percentage of \bar{b});
- mean height (\bar{h}_{NEP});
- number of particles (N_p);
- cover rate $TDC = (\sum S_{floor})/S$;
- $P_{fric} = TDC \cdot (S_{frontal}/S_{floor})$;
- $1 - R_{fric}$ directly assessed from numerical computations of the mean friction velocity on the erodible surface (u_r^*);

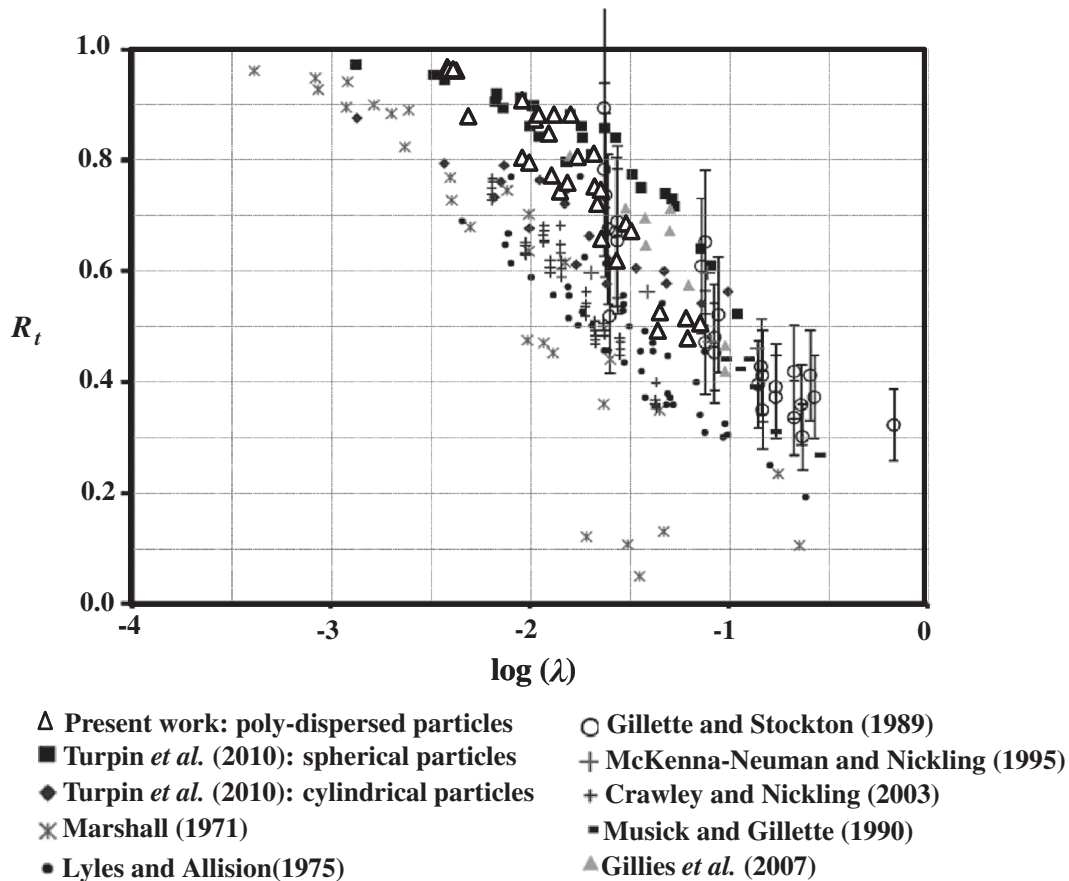


Figure 2. Comparison of the friction velocity ratio R_t from various sources (Marshall, 1971; Lyles and Allison, 1975; Gillette and Stockton, 1989; Musick and Gillette, 1990; McKenna-Neuman and Nickling, 1995; Crawley and Nickling, 2003; Gillies *et al.*, 2007; Turpin *et al.*, 2010) with those from the numerical simulations presented in this paper. Error bars 20% represent the accuracy of the Gillette and Stockton (1989) data.

- $1 - R_{fric}$ calculated with the formulation proposed by Turpin *et al.* (2010) (Equation (2)).

To define a test case, a random sampling of diameters (among the possible values established in the range) and height values of each particle is done. A cover rate for the test is also specified. A routine developed for the construction of numerical cases stops the sampling of particles as the defined cover rate value is reached.

Since the particles do not present the same diameter and height we must choose a mean value of S_{front}/S_{floor} to be representative of this distribution and to be replaced in the formulation of Turpin *et al.* (2010) (Equation (2)). The mean value of the parameter S_{front}/S_{floor} may be calculated in two ways: $\overline{S_{front}/S_{floor}}$ or S_{front}/S_{floor} . A maximum difference of 5% was found among the overall tested cases. Finally, a second approach was chosen: $\overline{S_{front}/S_{floor}}$. Table IV details the sampling for a given configuration (test 11). The accumulation of cover rate after each random sample, the dimensions and the computed values of S_{front} and S_{floor} are presented.

Results and discussion

The results section is divided in two parts. First, the discussion concerns comparisons between numerical results of previous (Turpin *et al.*, 2010) and present works to test the relevance of Equation (2) using non-uniform particles. The second part analyses the flow characteristics over the flat bed of non-uniform particles: distribution of wall shear stress, fluid flow patterns surrounding the various particles and roughness wind velocity profile for smooth and rough simulations.

Analysis of the validity of uniform formulation for non-uniform configurations

The main purpose of this section is the evaluation of the mathematical formulation initially proposed for uniform particles (Equation (2)). The evaluation will be carried out by a comparison between the values calculated with Equation (2) and the results of numerical simulations of non-uniform configurations done for this work (cf. Table III). The aim is to check whether the same representation in the non-uniform cases can be used.

Figure 3 presents two plots: Figure 3a shows the evolution of $1 - R_{fric}$ versus the parameter $P_{fric} = TDC \cdot (S_{front}/S_{floor})$ computed by the two approaches mentioned above and Figure 3b shows the correlation between these values of $1 - R_{fric}$.

As shown in the plot, the formulation is well founded enough to represent a wide range of particle diameters and height distribution. Figure 3 shows good agreement between the formulation and the numerical results when applied to non-uniform particles (Figure 3a), with a high correlation $R^2 = 0.9917$ (Figure 3b). The break in the slope is observed in the same way for the non-uniform configuration numerical simulation results (Figure 3a).

Analysis of fluid flow over roughness elements

The second part of this section presents a focus on the fluid flow characteristics for various cases. Top and three-dimensional visualizations illustrate the distribution of wall shear stress over the erodible surface surrounding the roughness elements. Also, the effects of the roughness elements on the mean velocity profile

Table I. Definitions of Symbols Used

Symbol	Units (SI)	Definition
$a_{p1}, m_{p1}, n_{p1},$ a_{p2}, m_{p2}, n_{p2}		Coefficients of Equation (2)
b	(mm)	Roughness element diameter
C_R		Roughness element drag coefficient
C_S		Surface drag coefficient
h	(mm)	Roughness element height
h_S	(mm)	Mean roughness elements height
m		Surface shear stress inhomogeneity parameter
N_p		Number of roughness elements
P_{fric}		Roughness element geometrical parameter (TDC. $S_{\text{floor}}/S_{\text{frontal}}$)
R_{fric}		Friction velocity ratio
R_t		Threshold friction velocity ratio
R		Correlation coefficient
S_{floor}	(mm ²)	Roughness element basal surface
S_{frontal}	(mm ²)	Roughness element frontal surface
S	(mm ²)	Computational domain basal surface
TDC		Cover rate (TDC = $(\sum S_{\text{floor}})/S$)
u_R^*	(m s ⁻¹)	Friction velocity for an erodible surface protected by roughness elements
u_S^*	(m s ⁻¹)	Friction velocity for a smooth erodible surface
u_t^*	(m s ⁻¹)	Threshold friction velocity
u_{t-R}^*	(m s ⁻¹)	Threshold friction velocity for an erodible surface protected by roughness elements
u_{t-S}^*	(m s ⁻¹)	Threshold friction velocity for a smooth erodible surface
x, y and z x^+, y^+, z^+, u^+ and h_S^+	(m)	Computational coordinates Coordinates, streamwise wind velocity and mean roughness height in wall units
β		Ratio of roughness element to surface drag coefficients
λ		Roughness density
ν	(m ² s ⁻¹)	Kinematic viscosity
ρ	(kg m ⁻³)	Air density
σ		Ratio of roughness element basal to frontal area ($S_{\text{floor}}/S_{\text{frontal}}$)
τ	(Pa)	Total shear stress
τ_R	(Pa)	Roughness element shear stress
τ_S	(Pa)	Surface shear stress
τ_{ref}	(Pa)	Reference shear stress computed over an erodible surface without roughness elements

are analysed comparing the velocity profile for various roughness configurations with that over a smooth wall. This section discusses the fluid flow features observed around the different emerging forms of the non-erodible particles.

Table II. Comparison of uniform configurations: present numerical simulations with *Code_Saturne* vs. Turpin *et al.* (2010) numerical simulations with Fluent

Test	N_p	b (mm)	h (mm)	TDC	$1 - R_{\text{fric}}$ Code_Saturne	$1 - R_{\text{fric}}$ Fluent
A	14	1.830	0.600	4.06	0.163	0.160
B	42	1.960	0.800	13.98	0.379	0.374
C	14	0.870	0.100	0.89	0.002	0.000

Top visualization of shear stress partitioning over the erodible surface

Figure 4 presents a plan view of shear stress distributions for four tested configurations. The cases were represented with the same scale of values. The values of wall shear stress are normalized by the value computed in the smooth case ($\tau_{\text{ref}} = 0.158 \text{ Pa}$).

Figure 4a presents the configuration with the smallest mean diameter (Test 13: $\overline{b}_{13} = 1.25 \text{ mm}$) among the tests shown in Figure 4. The range of diameters is also small (between 1.0 and 1.5 mm), which means a test close to the uniform distribution. The number of particles ($N_b = 51$) is among the most elevated of the overall tested configurations and the cover rate reaches almost 7%. The range of particle heights is important (between 10% and 45% of \overline{b}). However, as the mean diameter is small, this configuration does not present any high emerging particles. Most of the surface shows normalized wall shear stress values (τ/τ_{ref}) of about 0.800. The highest wall friction values are found on the detachment points of the most emerged particles. Test 13 presents only very small zones, with the normalized wall shear stress around 1.700. Moreover, the arrangement of the roughness elements in this configuration is characterized by small diameters, large number and magnitude of gaps between the elements and free zones on the erodible surface. Accordingly, the known effects of wakes on the erodible surface (diminution of the overall erosion) are reduced for this configuration.

Figure 4b represents Test 15. This configuration has been chosen for comparison with both Tests 13 (Figure 4a) and 16 (Figure 4c). First, it can be noted that Tests 13 and 15 present similar cover rate values (6.67% and 5.98%, cf. Table III). However, the parameter P_{fric} is higher for Test 15, which induces an increase of the value of $1 - R_{\text{fric}}$ (from 0.161 for Test 13 to 0.190 for Test 15). Also, it shows a slight diminution of the mean rough friction velocity (from 0.3012 to 0.2909).

In Test 15, although observing larger wake zones downstream and particles of greater diameter (vs. Test 13), higher maximum values of the normalized wall shear stress are reached. The wakes of the larger particles (high diameter values) normally have the main impact on the reduction of overall erosion. However in this case, some of these larger particles are located in the wake of upstream particles (in the lower left of Figure 4b) and therefore have weaker reducing impacts. On the other hand, particles positioned transversely to the flow direction (upper left of Figure 4b) produce a very large area of protection inducing a reduced wall friction.

Test 16 in Figure 4c presents a mean rough friction velocity very close to Test 15 (0.2910 and 0.2909, respectively). However, the ranges of diameter and height, as well as the cover rate, are quite different. This comparison is then interesting in showing the influence of each parameter on the modifications of the friction velocity on the erodible surface. Test 16 has a higher cover rate, normally resulting in a reduction of the mean friction velocity. On the other hand, Test 16 presents more elevated emerging particles, which lead to higher zones with normalized wall shear

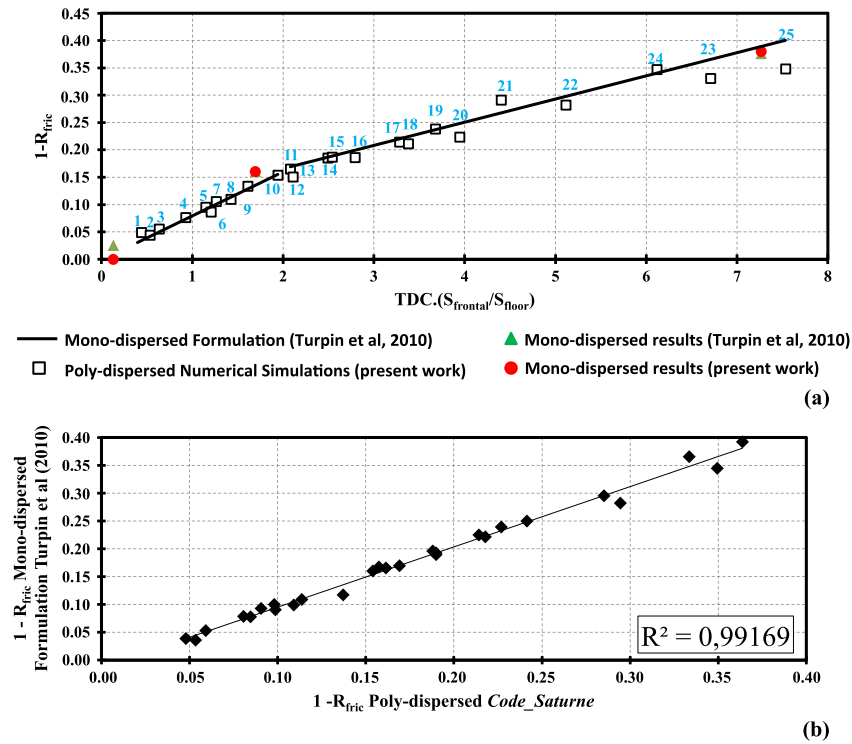


Figure 3. Parameter $1 - R_{fric}$: (a) $1 - R_{fric}$ calculated by the present numerical simulations and $1 - R_{fric}$ calculated with the formulation proposed by Turpin *et al.* (2010) and (b) correlation between $1 - R_{fric}$ compared with the formulation of Turpin *et al.* (2010) and with the results of the numerical simulations R is the value of the correlation coefficient. This figure is available in colour online at wileyonlinelibrary.com/journal/espl

stress close to the maximum. In addition, Test 15 with a smaller cover rate presents larger particles than Test 16, which possibly increases wake zones and reduces the mean friction velocity.

Finally, Figure 4d shows a high agglomeration of non-erodible particles (Test 25). The greater part of the erodible

surface shows a normalized shear stress lower than 0.250. The cover rate is highest (12.45%) among the overall tested configurations. Furthermore, due to the presence of high particles, the agglomeration of wakes has more influence on the overall distribution of wall shear stress.

Table III. Tested configurations

Test	b (mm)	\bar{b} (mm)	h (%) (\bar{b})	\bar{h} (mm)	N_p	TDC	P_{fric}^*	u_r^* (m s ⁻¹)	$1 - R_{fric}^{**}$	$1 - R_{fric}^{***}$
1	0.5–1.0	0.75	20–50	0.263	20	0.97	0.396	0.3415	0.049	0.032
2	0.5–1.5	1.00	10–30	0.200	18	2.01	0.536	0.3419	0.048	0.039
3	0.5–1.0	0.75	20–50	0.263	23	1.38	0.636	0.3379	0.059	0.053
4	0.5–1.0	0.75	20–50	0.263	43	2.05	0.927	0.3302	0.081	0.079
5	1.5–2.0	1.75	10–30	0.350	15	3.88	1.149	0.3237	0.099	0.090
6	0.7–1.7	1.20	10–40	0.300	34	4.13	1.206	0.3266	0.091	0.093
7	0.5–1.0	0.75	20–50	0.263	52	2.58	1.226	0.3239	0.098	0.100
8	1.0–1.5	1.25	10–30	0.250	42	5.87	1.426	0.3183	0.114	0.109
9	2.5–3.5	3.00	10–20	0.450	11	8.44	1.611	0.3099	0.137	0.118
10	0.5–1.5	1.00	20–50	0.350	46	4.16	1.942	0.3026	0.157	0.168
11	1.0–3.0	2.00	20–45	0.650	11	4.64	2.088	0.2984	0.169	0.169
12	0.7–1.7	1.20	10–40	0.300	54	6.57	2.111	0.3419	0.154	0.160
13	1.0–1.5	1.25	10–45	0.333	51	6.67	2.163	0.3012	0.161	0.165
14	1.0–2.0	1.50	40–50	0.675	20	4.32	2.492	0.2916	0.188	0.196
15	1.0–3.0	2.00	25–45	0.700	14	5.98	2.542	0.2909	0.190	0.190
16	1.5–2.0	1.75	05–50	0.481	25	8.51	2.793	0.2910	0.190	0.193
17	0.7–1.7	1.20	20–50	0.420	56	7.28	3.279	0.2809	0.218	0.222
18	1.0–3.0	2.00	20–40	0.600	25	8.14	3.379	0.2822	0.214	0.225
19	2.0–2.5	2.25	40–50	0.750	15	6.50	3.678	0.2724	0.242	0.250
20	1.0–3.0	2.00	10–50	0.600	34	11.67	3.945	0.2776	0.227	0.239
21	1.0–3.0	2.00	45–50	0.950	22	7.28	4.404	0.2534	0.294	0.282
22	0.9–2.9	1.90	20–50	0.665	34	11.72	5.114	0.2567	0.285	0.295
23	0.5–2.5	1.50	45–50	0.713	54	11.03	6.706	0.2394	0.333	0.365
24	1.3–1.8	1.50	45–50	0.713	53	10.16	6.116	0.2336	0.350	0.345
25	1.8–2.0	1.88	45–50	0.891	40	12.45	7.532	0.2285	0.364	0.392

* $P_{fric} = S_{frontal}/S_{floor} \cdot TDC$

**Present numerical simulations

***Turpin *et al.* (2010), (Equation (2))

Smooth friction velocity: $u_s^* = 0.3591$ m s⁻¹

Table IV. Summary of particles of Test 11 with $\bar{b}=2.00$, $\bar{h}_{NPE}=0.650$ and $P_{fric}=2.088$

Element	b (mm)	h (mm)	$S_{frontal}$	S_{floor}	$S_{frontal}/S_{floor}$	Accumulated TDC
1	1.14	0.39	0.45	1.02	0.44	0.11
2	1.86	0.83	1.54	2.72	0.57	0.42
3	2.39	0.91	2.18	4.47	0.49	0.91
4	2.71	0.66	1.78	5.75	0.31	1.55
5	2.74	1.05	2.88	5.90	0.49	2.21
6	1.17	0.42	0.49	1.08	0.46	2.33
7	2.68	1.16	3.12	5.65	0.55	2.96
8	2.43	0.98	2.38	4.65	0.51	3.47
9	2.56	0.76	1.93	5.13	0.38	4.04
10	2.04	0.65	1.33	3.28	0.41	4.41
11	1.65	0.44	0.73	2.15	0.34	4.64

$$\overline{S_{frontal}/S_{floor}} = 0.45$$

$$TDC = 4.64\%$$

$$1 - R_{fric} = A \cdot (TDC)^M \cdot (S_{frontal}/S_{floor})^N = 0.123(4.64^{0.613})(0.45^{0.77}) = 0.169.$$

Lee and Soliman (1977) have classified the flow over roughness elements with the values of the cover rate. Two regimes have been identified: isolated roughness flow ($TDC < 8$) and wake interference flow ($8 < TDC < 44$). Based on these definitions, Tests 13 and 15, previously presented in Figure 4, represent two cases of isolated roughness flow. Tests 16 and 25 belong to the wake interference flow regime. However, our work suggests that there is not a direct link between the flow regime and the erosion potential of a bed of particles.

Indeed, it has been shown previously, for uniform configurations (Turpin *et al.*, 2010), that an increase in roughness proportion, i.e. increase of the parameter P_{fric} , causes a decrease in the mean friction velocity. Our study confirmed that statement for non-uniform configurations. Nevertheless, this conclusion is not true for the cover rate (TDC) itself, as other geometry

parameters also influence the final value of the mean friction velocity. For instance, Test 15, in which cover rate is 5.98% and lower than that for Test 13, presents a slightly lower mean friction velocity. However, Test 15 presents a mean particle diameter of about twice that used in Test 13, which causes the protection zones to increase in size, and consequently a reduction in the mean friction velocity.

Three-dimensional visualization of fluid flow over roughness elements

Three-dimensional visualizations are presented in Figure 5. The differences observed in the roughness element dimensions may explain the important differences in wall shear stress results. Figure 5a, presenting Test 9, contains particles with very low heights, but with large diameters. This means a low value of

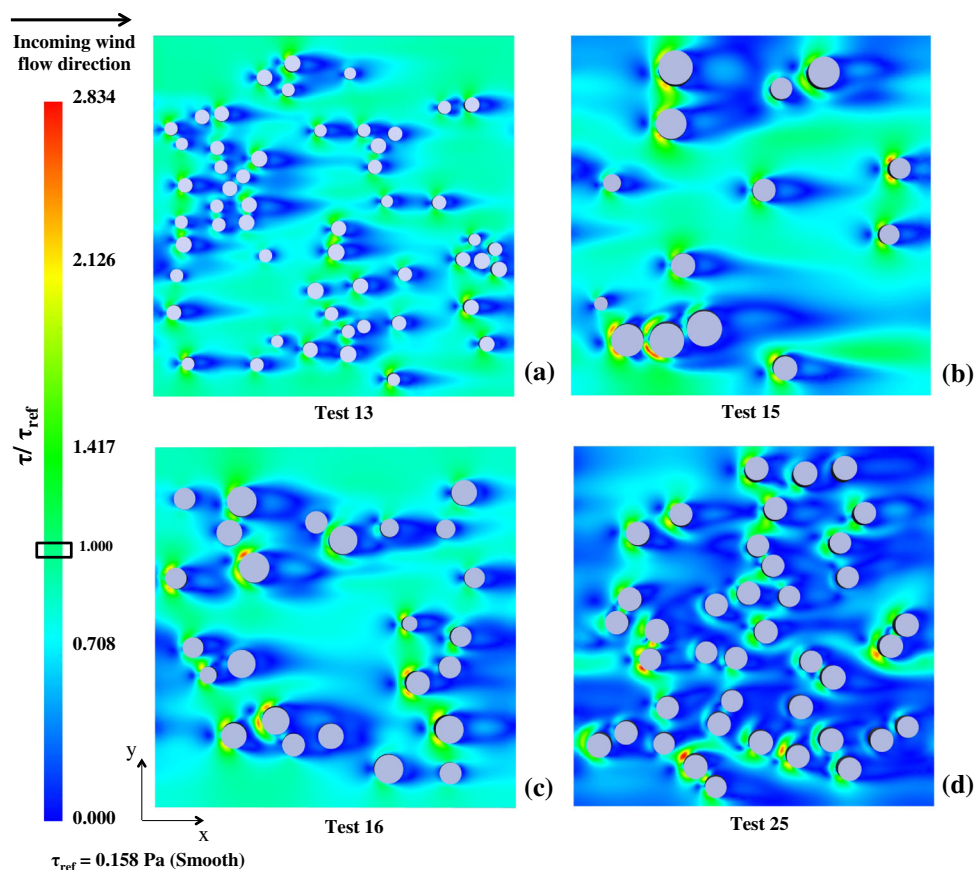


Figure 4. Distribution of non-dimensional wall shear stress over the erodible surface surrounding the roughness elements: (a) Test 13; (b) Test 15; (c) Test 16; (d) Test 25. This figure is available in colour online at wileyonlinelibrary.com/journal/espl

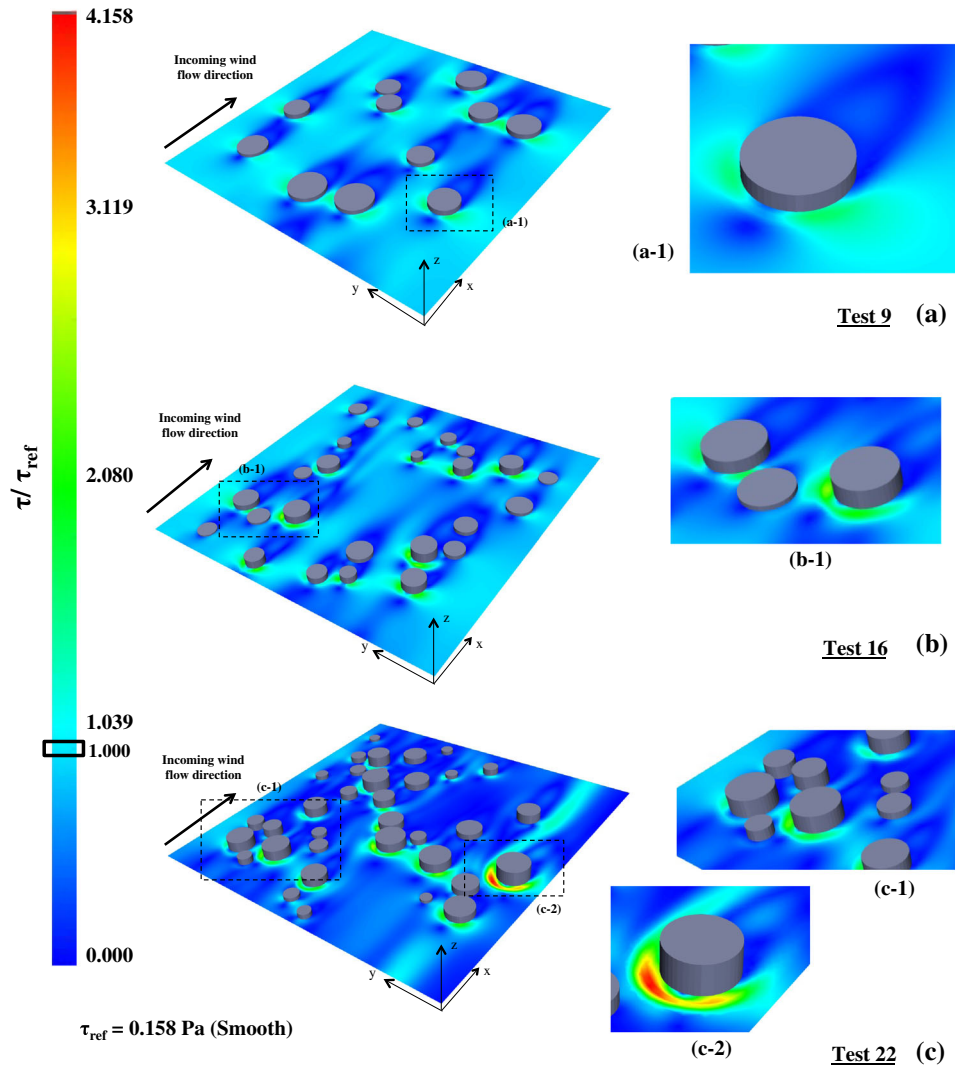


Figure 5. Three-dimensional view for three tested cases – distribution of non-dimensional wall shear stress with focus on specific roughness elements: (a) Test 9; (b) Test 16; (c) Test 22. This figure is available in colour online at wileyonlinelibrary.com/journal/espl

the parameter $\overline{(S_{\text{frontal}}/S_{\text{floor}})} = 0.190$ (cf. Table III). The highlighted region a-1 shows the detail of the wall shear stress distribution surrounding a particle. The normalized shear stress around this particle is not greater than 2.000. Even the particles which are not placed in the wake of other elements do not present high levels of wall shear stress. Despite the low level of shear stress computed around each single particle, it can be noted that for a significant extended area of the underlying erodible surface the mean normalized wall shear stress is greater than 1.000, which means erosion levels higher than the smooth case.

Test 16 in Figure 5b shows larger wake zones compared to Test 9 for some particles. Assisted by the highlighted region b-1, one can identify the variability of the influence on shear stress caused by the roughness height. These three particles have almost the same diameter. The level of the normalized shear stress on the wall surrounding each particle increases with the increase in height.

The distribution of Test 16 has an overall mean height much higher than Test 9. This causes an increase of the parameter $\overline{(S_{\text{frontal}}/S_{\text{floor}})}$. By applying Equation (2) this leads to a higher value of $1 - R_{\text{fric}}$ for the same cover rate, which is verified in the simulations. Concerning the shear stress distribution, particles with larger diameters exhibit an expanded region over them with an increase in shear stress. Therefore, one can observe higher mean friction velocities for Test 16.

For Test 22 (Figure 5c), the wake zones are the largest. Furthermore, two highlighted regions are noted. Region c-1 shows an agglomeration of roughness elements and the formation of a high wake with the lowest levels of normalized wall shear stress. Region c-2 exhibits the pattern found out over a highly emerged particle. The effects of a main vortex formed around the highlighted particle are noticed over the entire represented domain.

Figures 6a, b and c, focused on Tests 9 and 22, present, respectively, streamlines at an XZ plane, streamwise component of the wall shear stress (τ_{xz}) and plot of the evolution of streamwise wall shear stress. In Test 9 a smaller roughness element is surrounded by low friction levels; there are no complex structures that could affect the ground surface (see the small peak upstream of the element in Figure 6c). On the other hand, in Test 22 the high area of the windward wall of the emerged particle promotes the formation of vortices (notably towards the left) that impact the ground region (Region B) and increase the velocity gradient and consequently the wall shear stress. Moreover, Figure 6b displays the distribution of the longitudinal component of the wall shear stress on the underlying surface surrounding the roughness elements. The values were normalized by the value computed for the smooth case (τ_{ref}). Near the windward wall of the highest particle (Region B) peaks of negative longitudinal wall shear stress values are observed ($\tau_{xz}/\tau_{\text{ref}} = -3.35$ in Figure 6c). Region B is indeed associated with negative

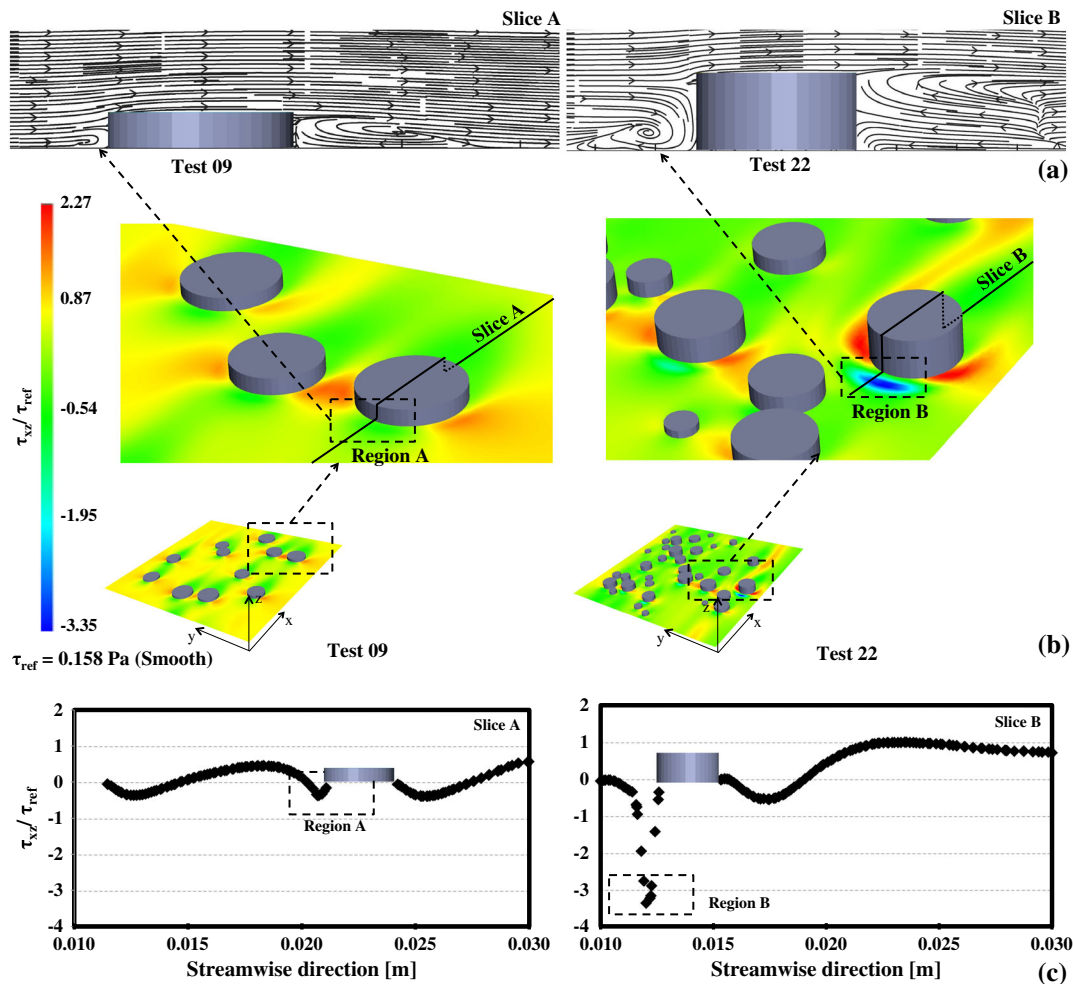


Figure 6. Local fluid flow modified due to the roughness elements for Test 9 and Test 22: (a) streamlines plotted on a XZ plane; (b) contours of the streamwise component of the wall shear stress; (c) evolution of the streamwise component of the wall shear stress. This figure is available in colour online at wileyonlinelibrary.com/journal/espl

values of X-velocity in Figure 6a. The roughness element highlighted in Test 9 shows a maximum negative value of $\tau_{xz}/\tau_{ref} = -0.50$ in Region A, which is very smaller than the value noticed in Region B.

Three-dimensional visualization allowed more local analysis of the turbulent fluid flow surrounding a roughness element with variability in their aspect ratios. The analyses have shown that the fluid flow passes over the low emerged particles without a main influence on the ground wall, whereas high emerged particles present strong shear stress levels on the windward wall with the creation of a main vortex which causes elevated friction on the ground wall. This analysis is useful to check the discussion of Figure 4 mainly concerning the influence of the emerging height.

Analysis of the vertical velocity profile for roughness elements immersed in a turbulent boundary layer
Numerical simulations of non-uniform non-erodible particles deal with the study of a turbulent boundary layer in the presence of roughness elements. Figure 7 plots mean velocity profiles (spanwise averaged) for Tests 5, 15 and 22 (see Table III) illustrating different cover rates and roughness proportions. The profiles of $u^+ = u/u^*$ and $z^+ = z \cdot u^*/\nu$ (respectively, longitudinal velocity and vertical coordinate, both calculated in wall units) are plotted. u^* is the mean shear velocity over the erodible and roughness elements surfaces for each test. The profiles are extracted at the same streamwise coordinate ($x = 0.0299$ m) close to the periodic boundary ($x = 0.03$ m).

The roughness height in wall units is defined by $h_s^+ = h_s u^* / \nu$. For the smallest value of cover rate (3.88 %, Test 5) and mean roughness height equal to 0.350 mm ($h_s^+ = 8.29$), the profile is the most similar to that over a smooth surface. Tests 15 and 22 present respectively a cover rate of 5.98% and 11.72% and mean roughness height of approximately 0.700 mm ($h_s^+ = 19.2$) and 0.665 mm ($h_s^+ = 18.97$). These values of h_s^+ indicate, for the three represented tested cases, that they are in transition regime where the roughness heights overpass the viscous sub-layer height which is highlighted in Figure 7.

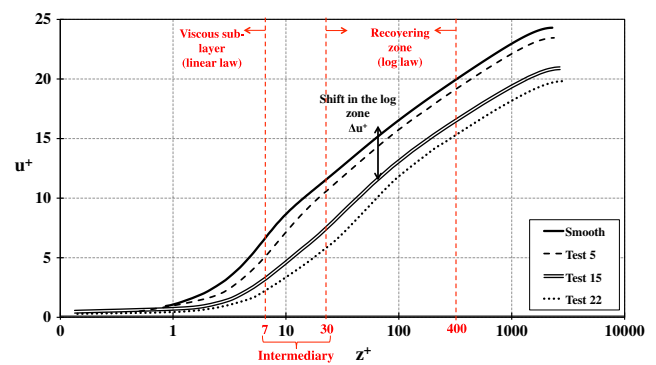


Figure 7. Vertical velocity profiles in wall units: comparison between the smooth configuration and different configurations of roughness elements. This figure is available in colour online at wileyonlinelibrary.com/journal/espl

For those configurations, the profiles are gradually distant ($\Delta u_5^+ < \Delta u_{15}^+ < \Delta u_{22}^+$). Thus Figure 7 illustrates that in comparison to the smooth pattern the effect of the roughness elements change is to the vertical profile (slope changes close to the wall) and also the height of the viscous sub-layer.

These numerical simulation results agree with the experimental work carried out by Clauser (1956). This reference work has defined the turbulent boundary layer in which roughness elements are immersed in the logarithmic zone of the velocity profile; the profiles must approach straight lines of slope close to 5.6 (Clauser, 1956), which can be seen in our tested cases. Moreover, it can be seen that, as the cover rate or roughness elements height increases there is a different transition between the logarithmic and the linear profile. As also remarked by Turpin *et al.* (2010) for their simulations, a distinct break in slope is observed close to the wall ($z^+ < 5$).

Conclusions

The main objective of this paper was the analysis of a mathematical formulation previously proposed in the open literature for quantification of the mean friction velocity evolution of a domain partially covered by roughness elements. These roughness elements represent non-erodible particles over an erodible surface. The above-mentioned formulation (detailed in the work of Turpin *et al.*, 2010) has been defined after some results of numerical simulations validated by experimental studies. However, the formulation was only representative of a bed of particles with equal diameters and heights, i.e. uniform distribution. On industrial sites and in the natural environment, this condition is very rarely encountered.

Thus several numerical simulations were carried out (with an open-source CFD code) to check the application of this formulation to non-uniform roughness elements (i.e. with different diameters and heights). The comparison has shown very good agreement. Some validations were additionally performed: three uniform configurations to compare the current simulations and those previously carried out, results of friction velocity ratio compared with various experimental and field simulations and modifications of the particle distribution to validate the domain dimensions. All comparisons and validations have presented good agreement.

A finer analysis of the numerical simulations results has shown that:

- the cover rate and the surface ratio ($S_{\text{frontal}}/S_{\text{floor}}$) are still (for a non-uniform distribution) the main parameters defining the evolution of the mean friction velocity over the erodible surface. The increase of their product (i.e. the parameter P_{fric}) leads to diminution of the mean friction velocity;
- the mean particle diameter presents a strong influence on the erosion of the ground surface due to the formation of more extended wake zones downstream of the roughness elements inducing the reduction of the erosion;
- the mean particle height presents a strong influence on the erosion of the ground surface due to the vortices potentially highly eroding the region around the roughness elements.

Finally, the present results state that the original formulation given by Turpin *et al.* (2010) is useful, without any modification in its form and coefficients, for a wide range of particles, with a random distribution and a large spectrum of dimensions. The application on fugitive dust emissions is then more refined due to the non-uniform numerical simulations carried out.

Acknowledgement—This work was carried out with the financial support of EDF R&D.

References

- Al-Awadhi JM, Willetts BB. 1999. Sand transport and deposition within arrays of non-erodible cylindrical elements. *Earth Surface Processes and Landforms* **24**: 423–435.
- Archambeau F, Mchitoua N, Sakiz M. 2004. Code Saturne: a finite volume code for turbulent flows. *International Journal on Finite Volumes* **1**(1), <http://www.latp.univ-mrs.fr/IJFV/spip.php?rubrique1>.
- Badr T. 2007. Quantification des émissions atmosphériques diffuses produites par érosion éolienne. Thèse de Doctorat, Université de Valenciennes et du Hainaut Cambrésis, Département Énergétique Industrielle, Ecole de Mines de Douai.
- Badr T, Harion J-L. 2007. Effect of aggregate storage piles configuration on dust emissions. *Atmospheric Environment* **41**: 360–368.
- Benkhaldoun F, Sari S, Seaid M. 2012. A flux-limiter method for dam-break flows over erodible sediment beds. *Applied Mathematical Modelling* **36**: 4847–4861.
- Bullard J, Austin M. 2011. Dust generation on a proglacial floodplain, West Greenland. *Aeolian Research* **3**: 43–54.
- Buynevich I. 2012. Morphologically induced density lag formation on bedforms and biogenic structures in aeolian sands. *Aeolian Research* **7**: 11–15.
- Carney SK, Bledsoe BP, Gessler D. 2005. Representing the bed roughness of coarse-grained streams in computational fluid dynamics. *Earth Surface Processes and Landforms* **31**: 736–749.
- Castel IY. 2006. A simulation model of wind erosion and sedimentation as a basis for management of a drift sand area in The Netherlands. *Earth Surface Processes and Landforms* **32**: 602–611.
- Clauser FH. 1956. The Turbulent Boundary Layer. Advances in Applied Mechanics, Vol. 4. Academic Press: New York.
- Crawley DM, Nickling WG. 2003. Drag partition for regularly arrayed rough surfaces. *Boundary-Layer Meteorology* **107**: 445–468.
- Davidson-Arnott GD, White DC, Ollerhead J. 1997. The effects of artificial pebble concentrations on eolian sand transport on beach. *Canadian Journal of Earth Sciences* **34**: 1499–1508.
- Ferreira A, Lambert R. 2011. Numerical and wind tunnel modeling on the windbreak effectiveness to control the aeolian erosion of conical stockpiles. *Environmental Fluid Mechanics* **11**: 61–76.
- Furieri B, Russeil S, Harion J-L, Turpin C, Santos J. 2012. Experimental surface flow visualization and numerical investigation of flow structure around an oblong stockpile. *Environmental Fluid Mechanics* **12**: 533–553.
- Gillette D, Stockton P. 1989. The effect of nonerodible particles on wind erosion of erodible surfaces. *Journal of Geophysical Research* **94**: 12885–12893.
- Gillies D, Nickling W, King K. 2007. Shear stress partitioning in large patches of roughness in the atmospheric inertial sublayer. *Boundary-Layer Meteorology* **122**: 367–396.
- Gimenez R, Leonard J, Duval Y, Richard G, Govers G. 2006. Effect of bed topography on soil aggregates transport by rill flow. *Earth Surface Processes and Landforms* **32**: 602–611.
- Guingo M, Minier J-P. 2008. A new model for the simulation of particle resuspension by turbulent flows based on a stochastic description of wall roughness and adhesion forces. *Journal of Aerosol Science* **39**: 957–973.
- Hugenholtz CH, Wolfe SA, Walker IJ, Moorman BJ. 2009. Spatial and temporal patterns of aeolian sediment transport on an inland parabolic dune, Bigstick Sand Hills, Saskatchewan, Canada. *Geomorphology* **105**: 158–170.
- Jiang Y, Matsusaka S, Masuda H, Qian Y. 2008. Characterizing the effect of substrate surface roughness on particle-wall interaction with the airflow method. *Powder Technology* **186**: 199–205.
- King J, Nickling WG, Gillies JA. 2005. Representation of vegetation and other nonerodible elements in aeolian shear stress partitioning models for predicting transport threshold. *Journal of Geophysical Research* **110**: F04015.
- Kurose R, Komori S. 2001. Turbulence structure over a particle roughness. *International Journal of Multiphase Flow* **27**: 673–683.
- Lee BE, Soliman BF. 1977. An investigation of the forces on three dimensional bluff bodies in rough wall turbulent boundary layers. *Journal of Fluids Engineering* **23**: 503–510.
- Li L, Martz L. 1995. Aerodynamic dislodgement of multiple size grains over time. *Sedimentology* **42**: 683–694.

- Lopez MV, Herrero JMD, Hevia GG, Gracia R, Buschiazio DE. 2007. Determination of the wind-erodible fraction of soils using different methodologies. *Geoderma* **137**: 407–411.
- Lyles L, Allison BE. 1975. Wind erosion: The protective role of simulated standing stubble. *American Society of Agricultural Engineering* **19**(1): 61–64.
- Marshall JK. 1971. Drag measurements in roughness arrays of varying density and distribution. *Agricultural Meteorology* **8**: 269–292.
- McKenna-Neuman C, Nickling W. 1995. Aeolian sediment flux decay: non-linear behaviour on developing deflation lag surfaces. *Earth Surface Processes and Landforms* **20**: 423–435.
- McKenna-Neuman C, Li B, Nash D. 2012. Micro-topographic analysis of shell pavements formed by aeolian transport in a wind tunnel simulation. *Journal of Geophysical Research – Earth Surface* **117**: F04003.
- Mountney N, Russell A. 2004. Sedimentology of cold-climate aeolian sand sheet deposits in the Askja region of northeast Iceland. *Sedimentary Geology* **166**: 223–244.
- Musick HB, Gillette DA. 1990. Field evaluation of relationships between a vegetated structural parameter and sheltering against wind erosion. *Land Degradation and Rehabilitation* **2**: 87–94.
- Neuman C. 1998. Particle transport and adjustments of the boundary layer over rough surfaces with an unrestricted, upwind supply of sediment. *Geomorphology* **25**: 1–17.
- Neuman C, Boulton J, Sanderson S. 2009. Wind tunnel simulation of environmental controls on fugitive dust emissions from mine tailings. *Atmospheric Environment* **43**: 520–529.
- Orlandi P, Leonardi S. 2008. Direct numerical simulation of three-dimensional turbulent rough channels: parametrization and flow physics. *Journal of Fluid Mechanics* **606**: 399–415.
- Raupach M, Gillette D, Leys J. 1993. The effect of roughness elements on wind erosion threshold. *Journal of Geophysical Research* **98**: 3023–3029.
- Roney J, White B. 2006. Estimating fugitive dust emission rates using an environmental boundary layer wind tunnel. *Atmospheric Environment* **40**: 7668–7685.
- Roney J, White B. 2010. Comparison of a two-dimensional numerical dust transport model with experimental dust emissions from soil surfaces in a wind tunnel. *Atmospheric Environment* **44**: 512–522.
- Schlichting H. 1968. *Boundary-Layer Theory* (7th edn). McGraw-Hill: New York.
- Shao Y, Yang Y. 2005. A scheme for drag partition over rough surfaces. *Atmospheric Environment* **39**: 7351–7361.
- Sutton SLF, Neuman CM. 2008. Sediment entrainment to the lee of roughness elements: effects of vortical structures. *Journal of Geophysical Research* **113**: F02S09.
- Taylor PA. 1988. Turbulent wakes in atmospheric boundary layer. In *Flow and Transport in the Natural Environment: Advances and Applications*, Steffen WL, Denmead OT (eds). Springer: Berlin; 270–292.
- Turpin C, Harion J-L. 2010. Effect of the topography of an industrial site on dust emissions from open storage yards. *Environmental Fluid Mechanics* **10**: 677–690.
- Turpin C, Badr T, Harion J-L. 2010. Numerical modelling of aeolian erosion over rough surfaces. *Earth Surface Processes and Landforms* **35**: 1418–1429.
- Webb N, Strong C. 2011. Soil erodibility dynamics and its representation for wind erosion and dust emission models. *Aeolian Research* **3**: 165–179.
- Zobeck T, Sterk G. 2003. Measurement and data analysis methods for field-scale wind erosion studies and model validation. *Earth Surface Processes and Landforms* **28**: 1163–1188.